Nano Research

Open Access

Research Article

High-selectivity direct electrooxidation of ethylene to ethylene glycol on an atomically precise silver cluster

Ya-Kun Lv[1,2], Meng-Yao Guo[1,2], Wen-Tao Liu[1,2], Yue-Ru Guo[1,2], Meng-Juan Wang[1,2], Jingzhen Du[1,2], Ren-Wu Huang[1,2] ✉, and Shuang-Quan Zang[1,2]

[1] *Henan Key Laboratory of Crystalline Molecular Functional Materials and College of Chemistry, Zhengzhou University, Zhengzhou 450001, China*
[2] *Key Laboratory of Special Functional Molecular Materials of Ministry of Education, Zhengzhou University, Zhengzhou 450001, China*

Cite this article: *Nano Research*, **2026**, *19*, 94908966. https://doi.org/10.26599/NR.2026.94908966

ABSTRACT: Electrochemical oxidation of ethylene (C_2H_4) to ethylene glycol (EG) offers a sustainable route for chemical production. However, designing catalysts at the atomic level and precisely elucidating the microscopic mechanisms of catalytic processes remain a formidable challenge. Here, we report a well-defined $Ag_{14}S(4\text{-}CF_3PhS)_{12}(PPh_3)_8$ cluster (Ag_{14}) and its electrocatalytic performance and mechanism for the conversion of C_2H_4 to EG. The Ag_{14} supported on carbon nanotubes (Ag_{14}/CNTs) achieved high selectivity (> 96%), EG productivity (73.43 μmol·h^{-1}), and turnover frequency (5.25 s^{-1}) at 2.4 V (vs. reversible hydrogen electrode). *In situ* characterization and theoretical calculations indicate that the catalytic process involves electrochemical activation of water to generate Ag-oxygen species, followed by the oxidation of C_2H_4 to form the intermediate ethylene oxide (EO), and eventually the ring-opening of EO to EG. The superior performance of Ag_{14}/CNTs is attributed to the role of mixed ligands in stabilizing high-valent silver and elevating the d-band centre, thereby reducing the adsorption free energy of key intermediates and suppressing the competing oxygen evolution reaction. This work provides a foundation for developing nano-sized silver-based catalysts for the electrocatalytic conversion of C_2H_4 to EG.

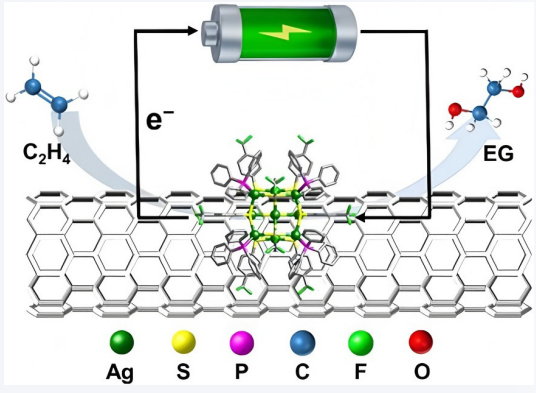

KEYWORDS: Ag clusters, precise structure, electrocatalysis, ethylene

1 Introduction

Ethylene (C_2H_4) oxidation is widely utilized in the chemical industry for the production of commodity chemicals, such as ethylene oxide (EO) and ethylene glycol (EG) [1–8]. In particular, EG, a fundamental chemical, serves as a critical precursor for producing a range of downstream products, including antifreeze, coolants, polyester, and electronic components [6–10]. By 2026, the global demand for EG is projected to exceed 77 million metric tons [10, 11]. In the industry, EG is produced through a two-step strategy involving catalytic C_2H_4 oxidation to EO and subsequent hydrolysis [12]. This route is energy-intensive, typically relying on temperatures of 200–300 °C and oxygen pressures of 1–3 MPa, emitting approximately 1.6 tons of CO_2 per ton of EG produced [13, 14]. Moreover, the harsh conditions of this route increase the risk of C_2H_4 peroxidation, resulting in low EG selectivity (overall below ~ 80%) [15]. Therefore, there is an urgent need to develop a more sustainable and cost-effective route for the oxidation of C_2H_4 to EG.

The electrochemical direct conversion of C_2H_4 to EG offers an attractive alternative, as it can be driven by renewable electricity and operated under mild conditions [3, 16–19]. Moreover, water serves as the oxygen source, avoiding the use of hazardous or costly oxidants [6, 9]. Recent studies have established proof-of-concept for this transformation. For instance, Lum and co-workers reported a gold-doped palladium (Pd) catalyst, achieving an EG Faradaic efficiency (FE) of 80% at a partial current density of 5.7 mA·cm^{-2} [19]. Duan et al. developed a Cl^--modified dendrite Pd catalyst, further increasing the FE to 92% and the partial current density to 18 mA·cm^{-2} [20]. However, the high prices and scarcity of precious metals may limit their scalability, underscoring the need to reduce reliance on noble-metal catalysts.

Silver (Ag) is a promising alternative metal element due to its high activity for C_2H_4 conversion and lower cost (approximately 30-

Received: April 23, 2026; **Revised:** May 24, 2026
Accepted: June 23, 2026

✉Address correspondence to renwuhuang@zzu.edu.cn

fold lower than Pd) [21, 22]. In industry, Ag-based catalysts are widely used for C_2H_4 epoxidation while suppressing complete combustion, owing to their moderate adsorption capacity for oxygen species [2]. Holbrook Wise et al. first demonstrated the feasibility of direct electrochemical C_2H_4 to EG conversion on a Ag electrode, although only a low current density (10^{-3} mA·cm^{-2}) was achieved [23]. In 2023, Tang et al. reported an Ag-doped Pd nanodendrite electrocatalyst, in which Ag accelerates the formation and desorption of EG by modulating *OH coverage and lowering the reaction energy barrier [24]. Despite these advances, previously reported traditional metallic particles or bulk materials typically suffer from issues such as low metal atom utilization and unclear active site structures, which not only increase catalyst costs but also hinder research into the structure-activity relationship. Therefore, the development of silver-based catalysts with high surface-to-volume ratios and precise structures is crucial for improving atom economy and accurately elucidating reaction mechanisms.

Atomically precise metal clusters, with diminutive size (1–3 nm), unique electronic structure, and high surface-to-volume ratio, serve as ideal models for investigating structure-property relationships [25–31]. The multi-metal atomic core of the metal clusters facilitates the regulation of their catalytic activity, offering greater flexibility compared to molecular or bulk catalysts [32–37]. Beyond the metal core, the electronic structure of catalytic sites in metal clusters can be specifically tuned by rationally designing the shell ligands, thereby improving catalytic performance [38–41]. In particular, a mixed-ligand strategy involving the co-protection of thiol and phosphine ligands can effectively stabilize the cluster and modulate its electronic structure to promote more favorable reaction pathways [30, 33]. These effects are particularly beneficial for multistep, multielectron processes like C_2H_4 to EG conversion, where the electron-donating effect of the ligand optimizes the valence state of Ag, thereby enhancing the reactivity of the Ag–O species [21, 22].

Herein, we synthesized an $Ag_{14}S(4\text{-}CF_3PhS)_{12}(PPh_3)_8$ clusters (Ag_{14}) using a mixed-ligand protection strategy and employed it as a model catalyst to study the electrocatalytic conversion mechanism of C_2H_4 to EG on nano-sized silver-based catalysts. As a result, the Ag_{14} supported on carbon nanotubes (Ag_{14}/CNTs) exhibits outstanding performance in the conversion of C_2H_4 to EG, with a productivity of 73.43 μmol·h^{-1}, high selectivity of > 96%, and turnover frequency (TOF) of 5.25 s^{-1} at 2.4 V (vs. reversible hydrogen electrode (RHE)). A combination of *in situ* characterization and theoretical calculations unveils that C_2H_4 is oxidized on the silver surface to form EO, which then spontaneously hydrolyzes to form EG. Furthermore, the electro-donating effect of mixed ligands effectively stabilizes the high-valent silver species and shift the d-band center upward, thereby lowering the rate-determining step (RDS) energy barrier and suppressing competitive oxygen evolution reactions (OER). This work confirms the critical role of ligands in metal clusters during the conversion of C_2H_4 to EG, providing new insights for the design of novel electrocatalysts.

2 Experimental

2.1 Preparation of the $(4\text{-}CF_3PhS)_nAg$

The $(4\text{-}CF_3PhS)_nAg$ precursors were synthesized using a method reported in the literature [42]. Specifically, 4.08 g $AgNO_3$ (24.0 mmol) was dissolved in a mixed solvent system comprising 150 mL of C_2H_5OH and 33 mL CH_3CN, and the mixture was stirred continuously at room temperature for 10 min to ensure complete dissolution. Subsequently, under light-proof condition, 0.8 mL of ($4\text{-}CF_3PhSH$) and 4.5 mL of Et_3N were slowly added dropwise to the resulting solution. The reaction was continued in the dark for 3 h, yielding a white precipitate. After completion, the precipitate was collected by vacuum filtration and washed sequentially with small portions of C_2H_5OH and CH_3CN. The resulting white solid was finally dried in a vacuum oven at 60 °C for 2 h to afford the target product as a white powder.

2.2 Preparation of the Ag_{14} NCs

$Ag_{14}(4\text{-}CF_3PhS)_{12}(PPh_3)_8$ was synthesized using a one-step solvothermal method. The precursor $(4\text{-}CF_3PhS)_nAg$ salt (20.0 mg) and PPh_3 (20.0 mg) were co-dissolved in a mixed solvent of CH_3CN (2 mL), p-xylene (0.5 mL), and DCM (2 mL) under ultrasonication. The resulting clear solution was then placed in an oven and heated at 60 °C for 72 h. Subsequently, it was cooled to room temperature at a rate of 2.5 °C·h^{-1}, yielding colorless hexagonal bulk crystals suitable for the single-crystal X-ray diffraction (SC-XRD) analysis.

2.3 Preparation of the Ag_{14}/CNTs

Briefly, 4.0 mg of Ag_{14} clusters were added to 30 mL of CH_2Cl_2 solution via ultrasonication for 10 min to disperse. Then, 20 mg of CNTs were added to the solution and the mixture was subjected to ultrasonication for 20 min. The mixture was stirred continuously at room temperature for 36 h to allow for the uniform adsorption and deposition of Ag_{14} onto the CNTs surfaces. Finally, the solvent was removed using a rotary evaporator to obtain a black solid powder of Ag_{14}/CNTs.

2.4 Preparation of the Ag NPs

A colloidal dispersion of silver nanoparticles was synthesized via a chemical reduction method. Briefly, 34 mg of $AgNO_3$ (0.2 mmol) was completely dissolved in 1 mL of absolute ethanol under ultrasonication for 5 min. Separately, an excess amount of PVP (100 mg) as a dispersing and stabilizing agent was dispersed in 2 mL of absolute ethanol. Under continuous magnetic stirring at room temperature, the PVP solution was added dropwise into the $AgNO_3$ solution, and the mixture was allowed to react for 20 min to facilitate the complexation between Ag^+ ions and PVP. Subsequently, a freshly prepared ethanolic solution of $NaBH_4$ (4 mg, 0.1 mmol) was introduced dropwise into the mixture. The system color transitioned from colorless to bright yellow, then to orange, and finally to dark brown, indicating the formation of Ag NPs. The resulting suspension was centrifuged and washed three times with water and ethanol.

2.5 Preparation of the Ag NPs/CNTs

The as-synthesized Ag NPs was diluted with 20 mL of ethanol, followed by the addition of CNTs (57 mg). The mixture was stirred continuously at room temperature for 36 h to allow for the uniform adsorption and deposition of Ag NPs onto the CNTs surfaces. Finally, the solvent was removed by rotary evaporation, yielding a black solid powder denoted as the Ag NPs/CNTs composite catalyst.

3 Results and discussion

3.1 Synthesis and characterization of catalysts

The fabrication process of the Ag_{14}/CNTs catalyst is schematically shown in Fig. 1(a). Firstly, Ag_{14} clusters were synthesized by one-pot solvothermal method. Briefly, $(4\text{-}CF_3PhS)_nAg$ (Fig. S1 in the

Electronic Supplementary Mterial (ESM)) and PPh_3 were added successively to a mixed solvent of CH_3CN, and CH_2Cl_2, which was then sealed and heated to 60 °C for 72 h. After cooling to room temperature, colorless crystals with a regular dodecahedral morphology were obtained (Fig. S2 in the ESM). SC-XRD shows that Ag_{14} clusters were crystallized in a trigonal space group $R\bar{3}$ with the molecular formula $Ag_{14}S(4\text{-}CF_3PhS)_{12}(PPh_3)_8$, an electrically neutral cluster (Fig. S3 and Tables S1 and S2 in the ESM). As shown in Figs. 1(b)–1(d), the Ag_{14} cluster has a distorted cubic geometry, with a maximum distance of 1.9 nm between its two most distant benzene-ring carbon atoms. Eight Ag atoms occupy the cube vertices, while the remaining six are located at the centres of the cube faces. The twelve sulfur atoms from the 4-CF_3PhS ligands bridge the cube edges. Each vertex Ag atom, bonded to one phosphine and three thiolate ligands, exhibits a distorted tetrahedral coordination configuration, whereas each face-centred Ag atom bridges two thiolate ligands and the central S^{2-} anion. The Ag_{14} clusters in the crystal are stacked together via hydrogen bonding (C-F···π) (Fig. S4 in the ESM). The fine phase purity of Ag_{14} clusters was further confirmed by well-matched powder X-ray diffraction (PXRD) pattern (Fig. 1(e)). In addition, we monitored the structural stability of the clusters using Ultraviolet–visible (UV–vis) spectroscopy. As shown in Fig. 1(f), the UV–vis absorption spectrum of Ag_{14} clusters remains stable for at least 48 h in CH_2Cl_2, providing reliable assurance of structural durability for potential catalytic behavior. We attempted to further characterize the molecular mass and composition of the Ag_{14} cluster by electrospray ionization mass spectrometry, but the neutral cluster ionizes poorly, preventing publishable results. The thermogravimetric (TG) curve indicates that Ag_{14} clusters exhibit high thermal stability up to 200 °C (Fig. S5 in the ESM). Moreover, the transmission electron microscopy (TEM) results confirmed that Ag_{14} clusters presented evenly dispersed character with a size of approximately 1.4 nm (Fig. 1(g)), which is particularly advantageous for the subsequent dispersion and loading of the clusters.

CNTs not only solve the problems of easy aggregation and poor conductivity of metal clusters but also significantly improve the overall catalytic activity and stability through electronic synergistic effects [43, 44]. To construct a composite system with a stable structure, efficient electron transport, and a synergistic catalytic effect, we loaded Ag_{14} clusters onto CNTs. Ag_{14} clusters and CNTs were thoroughly mixed in CH_2Cl_2, and the solvent was removed under reduced pressure to obtain Ag_{14}/CNTs. In contrast, Ag NPs/CNTs were also fabricated using a two-step method (see details in the Experimental section). PXRD of Ag_{14}/CNTs shows only a dominant broad peak at 25° (from CNTs), indicating that the Ag_{14} clusters are well dispersed on the CNTs (Fig. 2(a)). For Ag NPs/CNTs, the two peaks at 38° and 44° are attributed to the (111) and (200) crystal planes of cubic Ag (PDF #04-0783), respectively. The X-ray photoelectron spectroscopy (XPS) was performed to study the surface element composition and local electronic structure of the Ag_{14}/CNTs. As shown in Fig. S6 in the ESM, the XPS survey spectrum shows that F, Ag, C, S, and P are dominant in Ag_{14}/CNTs. In addition, the Ag 3d XPS spectra of Ag_{14}/CNTs and Ag_{14} clusters show two major peaks centered at 872.97 (Ag $3d_{3/2}$) and 854.77 eV (Ag $3d_{5/2}$), corresponding to approximately the +1

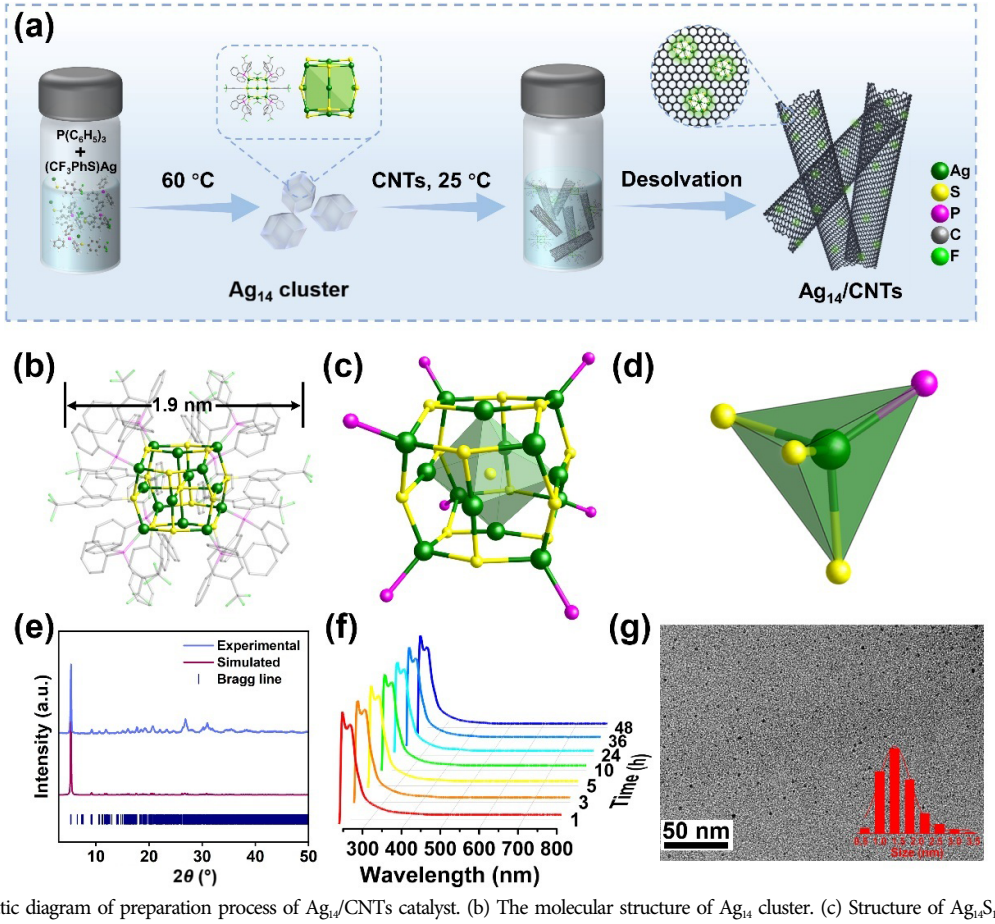

Figure 1 (a) Schematic diagram of preparation process of Ag_{14}/CNTs catalyst. (b) The molecular structure of Ag_{14} cluster. (c) Structure of $Ag_{14}S_{12}P_8$. (d) Coordination mode of the Ag atom in the Ag_8 cube. (e) PXRD, (f) time-dependent UV-vis spectra, and (g) TEM image of Ag_{14} clusters.

oxidation state (Fig. 2(b)) [45]. X-ray absorption spectroscopy was applied to further investigate the electronic structure of Ag_{14}/CNTs. The X-ray absorption near edge structure (XANES) spectra of Ag L-edge reveal that the energy absorption threshold value of Ag_{14}/CNTs is close to that of Ag_2O, further confirming that the valence of Ag atoms is close to +1. Precisely, the average oxidation state of Ag was calculated as +0.87 based on the adsorption threshold energies (Fig. S7 in the ESM). High-angle annular dark-field scanning transmission electron microscopy (HAADF-STEM) and its aberration-corrected variant reveal well-dispersed clusters on CNTs, with diameters of approximately 1.8 nm-consistent with the Ag_{14} size determined by X-ray crystallography (Figs. 2(d) and 2(e)). In addition, the energy dispersive spectroscopy (EDS) mapping showed that the Ag and S elements are uniformly distributed within the cluster regions, consistent with crystal observations, further confirming our successful preparation of Ag_{14} clusters with highly uniform distribution on CNTs (Fig. 2(f) and Fig. S8 in the ESM). F and P did not show regional distribution patterns, owing to their low abundance and small atomic masses. For Ag NPs/CNTs, Ag NPs with a larger size of approximately 9.0 nm were also identified by HAADF-STEM and EDS mapping (Figs. S9 and S10 in the ESM).

3.2 Electrocatalytic performance

The catalytic performance of Ag_{14}/CNTs in the electrochemical oxidation of C_2H_4 was investigated. For comparison, the catalytic activities of Ag_{14} clusters, CNTs, and Ag NPs/CNTs were also measured under the same conditions. The reaction was carried out in a high-pressure electrochemical cell equipped with a three-electrode system at room temperature (Fig. S11 in the ESM). Firstly, the typical linear sweep voltammetry (LSV) curves of Ag_{14}/CNTs, Ag_{14}, and Ag NPs/CNTs under different C_2H_4 pressures were obtained to investigate the correlation between C_2H_4 electrooxidation activity and pressure. As shown in Fig. 3(a) and Fig. S12 in the ESM, current density of both Ag_{14}/CNTs and pure Ag_{14} clusters first increasing and then decreased with increasing C_2H_4 pressure, reaching a maximum at 2 MPa. For Ag NPs/CNTs, the current density decreased slightly after the introduction of C_2H_4, and the current densities at different pressures were essentially the same. Therefore, all subsequent experiments were conducted at a C_2H_4 pressure of 2 MPa unless otherwise specified. The electrochemical performances of the as-prepared catalysts for the C_2H_4 to EG at different constant voltages were carried out, and the liquid products were analyzed. For Ag_{14}/CNTs (Fig. 3(b)), an EG productivity of 10.98 μmol·h^{-1} was observed at an applied potential of 2.2 V (vs. RHE), and the productivity continued to increase with the increase of potential, reaching 95.13 μmol·h^{-1} at 2.6 V (vs. RHE). In addition, the FE of Ag_{14}/CNTs varies in a volcano-like pattern with the change of potential, and it reaches its maximum value of ~ 29% with an EG partial current density of 3 mA·cm^{-2} at 2.4 V (Fig. 3(c) and Fig. S13 in the ESM). Note that the productivity and FE of Ag_{14}/CNTs were significantly higher than those of the other comparison samples over a wide potential range, demonstrating an absolute performance advantage. Conversely, the correlation between pressure and catalytic activity was further investigated at the optimum potential of 2.4 V (vs. RHE). As shown in Fig. S14 in the ESM, Ag_{14}/CNTs exhibited the highest productivity and FE at 2 MPa, consistent with the findings observed in the LSV. Although Ag_{14}/CNTs exhibits the highest FE at 2.4 V (vs. RHE), its significant potential for performance improvement remains to be explored. Thus, all other products were further analyzed to identify undesirable Faraday reactions occurring during the C_2H_4 to EG conversion, which might guide the rational design of advanced Ag-based catalysts. Regarding the liquid byproducts over Ag_{14}/CNTs, the acetaldehyde (AA), acetic acid (AcOH), and EO were observed but with trace FE (Fig. S15 in the ESM). We further attempted to analyze the products using differential electrochemical mass spectrometry (DEMS). The m/z = 32, 44, 60, 62 were observed, which were attributed to AA, AcOH, EO/CO_2, and EG, respectively (Fig. 3(d)). For the gas CO_2, it may be generated by CNTs and carbon paper on the electrodes according to the literature [15]. Therefore, we introduced N_2 into the reaction chamber to replace C_2H_4 and conducted the electrochemical reaction. Surprisingly, the

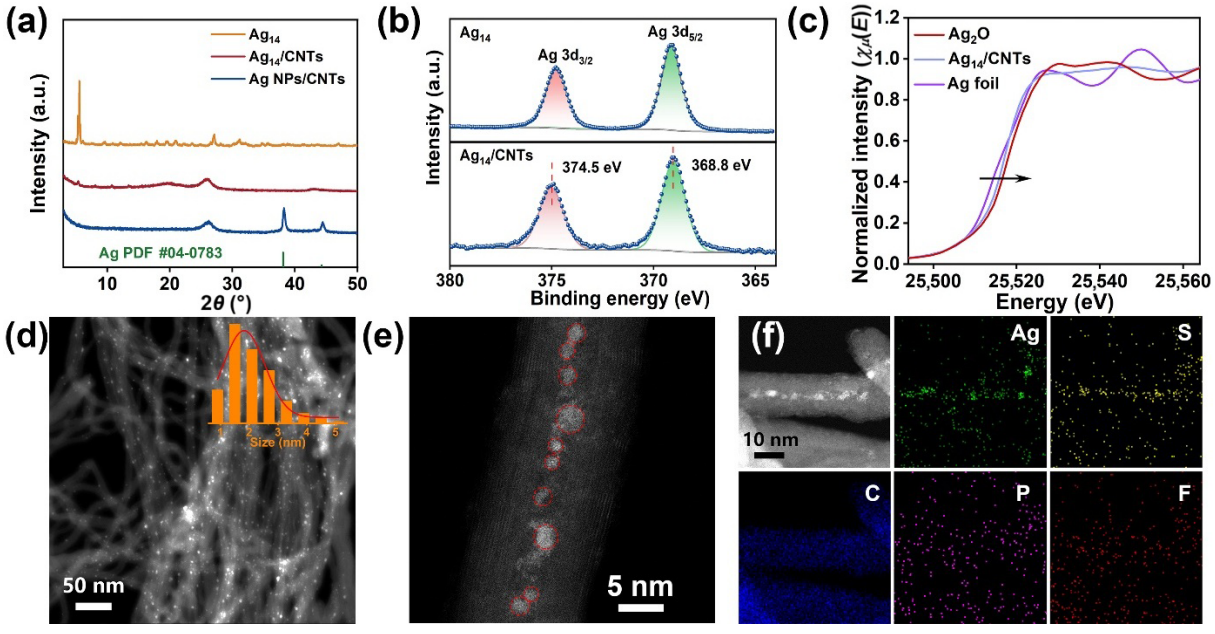

Figure 2 (a) The PXRD of Ag_{14}/CNTs and control samples. (b) High-resolution XPS spectra of Ag_{14} and Ag_{14}/CNTs. (c) Ag L-edge XANES spectra, (d) HAADF-STEM, (e) AC HAADF-STEM, and (f) EDS mapping of Ag_{14}/CNT.

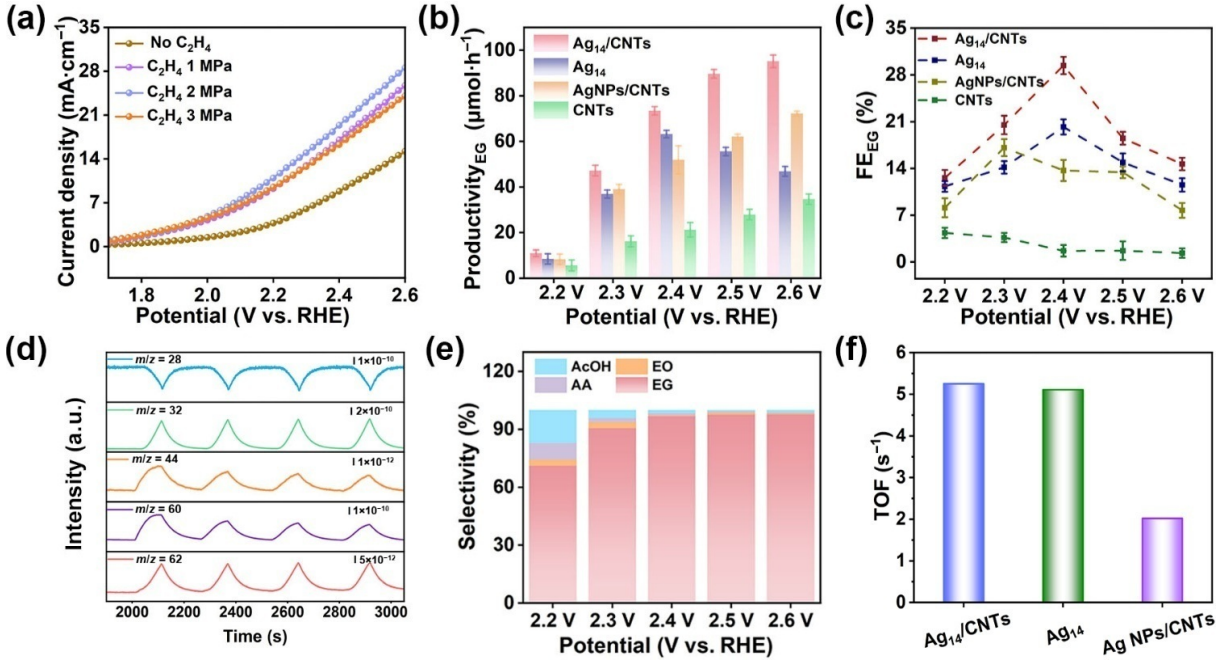

Figure 3 (a) LSV curves of Ag_{14}/CNTs with different C_2H_4 pressure. (b) Productivity and (c) Faraday efficiency of Ag_{14}/CNTs and control samples at different potentials. (d) DEMS analysis of Ag_{14}/CNTs in electrocatalytic C_2H_4 to EG process. (e) The selectivity and (f) TOF of Ag_{14}/CNTs and control samples.

FE of CO_2 produced in the N_2 environment is higher than that in the C_2H_4 environment at same applied potential (Fig. S16 in the ESM). This result indicates that the CO_2 during the reaction primarily originated from CNTs and carbon paper, and the involvement of C_2H_4 could suppress the peroxidation of the carbon support. Therefore, a high EG selectivity of > 96% (Fig. 3(e)), a FE of 29%, and productivity of 73.43 μmol·h^{-1} were determined when the potential was set to 2.4 V (vs. RHE). In addition, we analyzed the O_2 generated during the reaction process, as the OER is the primary competing reaction for C_2H_4 to EG conversion. As shown in Fig. S17 in the ESM, the FE for O_2 evolution using Ag_{14}/CNTs and Ag NPs/CNTs is 66.42% and 85.5%, respectively. The lower FE of O_2 evolution for Ag_{14}/NPs indicates its superior ability to suppress the OER during the C_2H_4 to EG conversion process compared to Ag NPs. To demonstrate this point, we performed LSV scans on Ag_{14}/CNTs and Ag NPs/CNTs in an N_2 atmosphere. In the Fig. S18 in the ESM, the overpotential of Ag_{14}/CNTs is significantly higher than that of Ag NPs/CNTs across the entire potential range, indicating that it exhibits lower OER activity. Furthermore, when comparing previously reported Pd dendrites, Pd-Ag, Ag networks, and commercial 20 wt.% Pd/C catalysts under the same experimental conditions (2 MPa C_2H_4, 2.4 V vs. RHE), the Ag_{14}/CNTs catalyst exhibited the highest productivity and a FE second only to that of the Pd-Ag catalyst (36.93%) (Fig. S19 in the ESM).

To qualify the intrinsic activity, the turnover frequencies (TOF) value was calculated based on the Pb underpotential deposition experiments (Fig. S20 in the ESM). As shown in Fig. 3(f), the TOF value of Ag_{14}/CNTs (5.25 s^{-1}) is comparable to that of Ag_{14} (5.11 s^{-1}) and significantly higher than that of Ag NPs/CNTs (2.02 s^{-1}). In addition, the electrochemical active surface areas (ECSA) of Ag_{14}/CNTs, Ag NPs/CNTs, and Ag_{14} were calculated 2.92, 5.3, and 2.53 cm^2, respectively (Fig. S20(b) in the ESM). Based on this, to further elucidate the origin of the performance improvement of Ag_{14}/CNTs compared to Ag NPs/CNTs, the double-layer capacitances (C_{dl}) were obtained by cyclic voltammetry (CV) curves. As shown in the Fig. 4(a) and Fig. S21 in the ESM, Ag_{14}/CNTs (10.20 mF·cm^{-2}) and Ag NPs/CNTs (9.86 mF·cm^{-2}) have comparable C_{dl} values, which are significantly higher than that of Ag_{14} clusters (3.80 mF·cm^{-2}). In addition, N_2 adsorption experiments indicate that Ag_{14}/CNTs and Ag NPs/CNTs have essentially the same specific surface area and pore size distribution (Fig. S22 in the ESM), indicating the enhanced catalytic activity of Ag_{14}/CNTs compared to Ag NPs/CNTs does not stem from an increase in active area. Therefore, the reaction kinetics of the as-catalysts were further analyzed via electrochemical impedance spectroscopy (EIS). As shown in Fig. 4(b), Ag_{14}/CNTs displayed the lowest arc radius among all catalysts, suggesting that Ag_{14}/CNTs possessed the lowest interfacial charge transfer resistance and the fastest reaction kinetics [46, 47].

Catalyst stability, critical for mechanistic studies and practical applications, was further evaluated. Quasi-*in situ* Raman spectroscopy characterized Ag_{14}/CNTs before and after the reaction. As shown in Fig. 4(c), the Raman spectrum of Ag_{14}/CNTs showed no observable changes across a wide potential range (2.2–2.6 V vs. RHE) after the electrochemical reaction, indicating that the Ag clusters underwent no noticeable structural transformation. The activity of the C_2H_4 to EG reaction remained at over 83% of the initial value after 8 h of electrolysis (Fig. 4(d)). In addition, the structure of Ag_{14}/CNTs after the catalytic reaction was characterized using XPS, UV–vis absorption spectra, and HAADF-STEM. As shown in Figs. S23(a) and S23(b) in the ESM, the post-reaction UV–vis absorption and valence state of the Ag clusters remain consistent with those before the reaction, indicating that the Ag_{14} structure has not undergone any significant changes. Furthermore, HAADF-STEM images reveal that the morphology and size of the Ag_{14} clusters on the CNTs have not undergone significant changes compared to their pre-reaction state (Figs. S23(c) and S23(d) in the ESM).

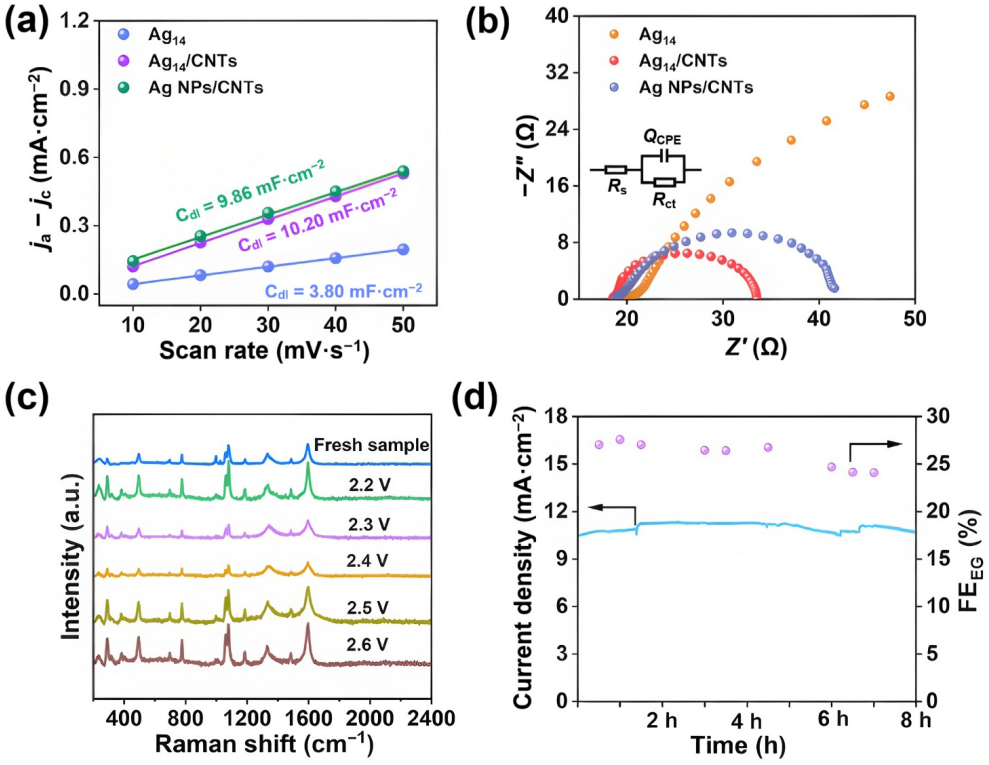

Figure 4 (a) The fitted linear relationship between current density and the scan rate, and (b) Nyquist plots for Ag_{14}/CNTs, Ag_{14}, and Ag NPs/CNTs. The inset shows the equivalent circuit. (c) Quasi-*in situ* Raman spectra of Ag_{14}/CNTs at different potentials. (d) Stability testing of Ag_{14}/CNTs.

3.3 Mechanism investigation

The reaction mechanism of Ag_{14}/CNTs for electrocatalytic C_2H_4 to EG conversion was studied by *in situ* Fourier transform infrared (FT-IR) test, which measured changes in intermediates and products under open-circuit potential (OCP) and reaction potential. The changes of intermediates and products in the reaction process under open circuit potential (OCP) and reaction potential were measured, respectively. In Fig. 5(a), as the potential increases from OCP to 2.4 V, some intermediate signal peaks were captured. The characteristic peaks at 1082.1 and 1122.1 cm^{-1} are assigned to the OCCO vibration of EG and the signature of EO, respectively [15, 20]. Note that the EO signal is stronger than the OCCO signal at the 2.0 V. However, the EO signal gradually decreases with increasing potential, while the OCCO signal gradually increases. This indicates that more EO desorbs from the catalyst surface and generates more EG. In addition, the characteristic peak of EO shifted from 1122.1 to 1116.4 cm^{-1}, meaning weaker adsorption of EO on the catalyst surface at higher potential [48]. The generation of H_2O_2 was excluded by conducting a $TiOSO_4$ titration experiment with the following UV–vis spectroscopy analysis (Fig. S24 in the ESM) [49]. Furthermore, no characteristic ·OH signal was observed in the electron paramagnetic resonance (EPR) spectrum, ruling out the possibility of ·OH directly oxidizing ethylene or contributing to the ring-opening of epoxyethane (Fig. S25 in the ESM). Therefore, it can be concluded that C_2H_4 is partially oxidized to EO on the catalyst surface and further hydrolyzed to EG. The detailed reaction steps are proposed (Fig. 5(b) in the ESM): First, H_2O molecules adsorb onto the Ag sites of Ag_{14} and undergo a gradual dehydrogenation process to form an Ag–O intermediate (steps 1–4), Next, C_2H_4 undergoes a cycloaddition reaction with the Ag–O intermediate to form EO (step 5). Finally, EO desorbs from the Ag surface and undergoes spontaneous hydrolysis to form EG (steps 6 and 7).

Density functional theory (DFT) calculations were performed to shed light on the origin of the superior catalytic activity of Ag_{14}/CNTs. Based on the SC-XRD analysis, the optimized configurations of Ag_{14}/CNTs were shown in Fig. S26(a) in the ESM. The Ag NPs/CNTs basic model was also built by anchoring face-centered cubic Ag on a carbon substrate (Fig. S26(b) in the ESM). The Gibbs free energy diagrams for different intermediates on both catalysts were shown in Fig. 5(c) and Figs. S27–S29 in the ESM. As for Ag_{14}/CNTs, the formation of *O from *OH was the RDS with a Gibbs energy difference of 1.16 eV, which was lower than that on Ag NPs/CNTs (1.35 eV). In addition, all the surface intermediates containing oxygen displayed a downhill energy change over Ag_{14}/CNTs, indicating that Ag_{14}/CNTs exhibit a faster EG formation rate. Notably, in the process of OER (Fig. S30 in the ESM), the transition from *O to O_2 was an RDS, and the energy barrier for Ag_{14}/CNTs (1.71 eV) was significantly higher than that for Ag NPs/CNTs (1.60 eV), indicating that the Ag_{14} clusters can effectively suppress the competitive OER (Figs. S31–S33 in the ESM).

To further investigate the mechanism of hybrid ligand–enhanced catalysis, we evaluated the electronic structures of various catalytic models. The calculated projected density of states (PDOS) indicated that the d-band center of $Ag_{14}(4\text{-}CF_3PhS)_{12}(PPh_3)_8$ (−2.93 eV) shifted closer to the Fermi level as compared to that of Ag NPs (−3.71 eV) (Fig. 5(d)). The results demonstrated the anti-bonding orbitals of Ag were less filled, which resulted in a stronger adsorption of reaction intermediates in $Ag_{14}(4\text{-}CF_3PhS)_{12}(PPh_3)_8$ [33, 50]. Furthermore, by removing the PPh_3 ligands from Ag_{14} cluster to obtain $Ag_{14}(4\text{-}CF_3PhS)_{12}$, we found that the d-band center of $Ag_{14}(4\text{-}CF_3PhS)_{12}$ (−3.24 eV) lies between those of Ag NPs and $Ag_{14}(4\text{-}CF_3PhS)_{12}(PPh_3)_8$, indicating that the upshift of the d-band center is

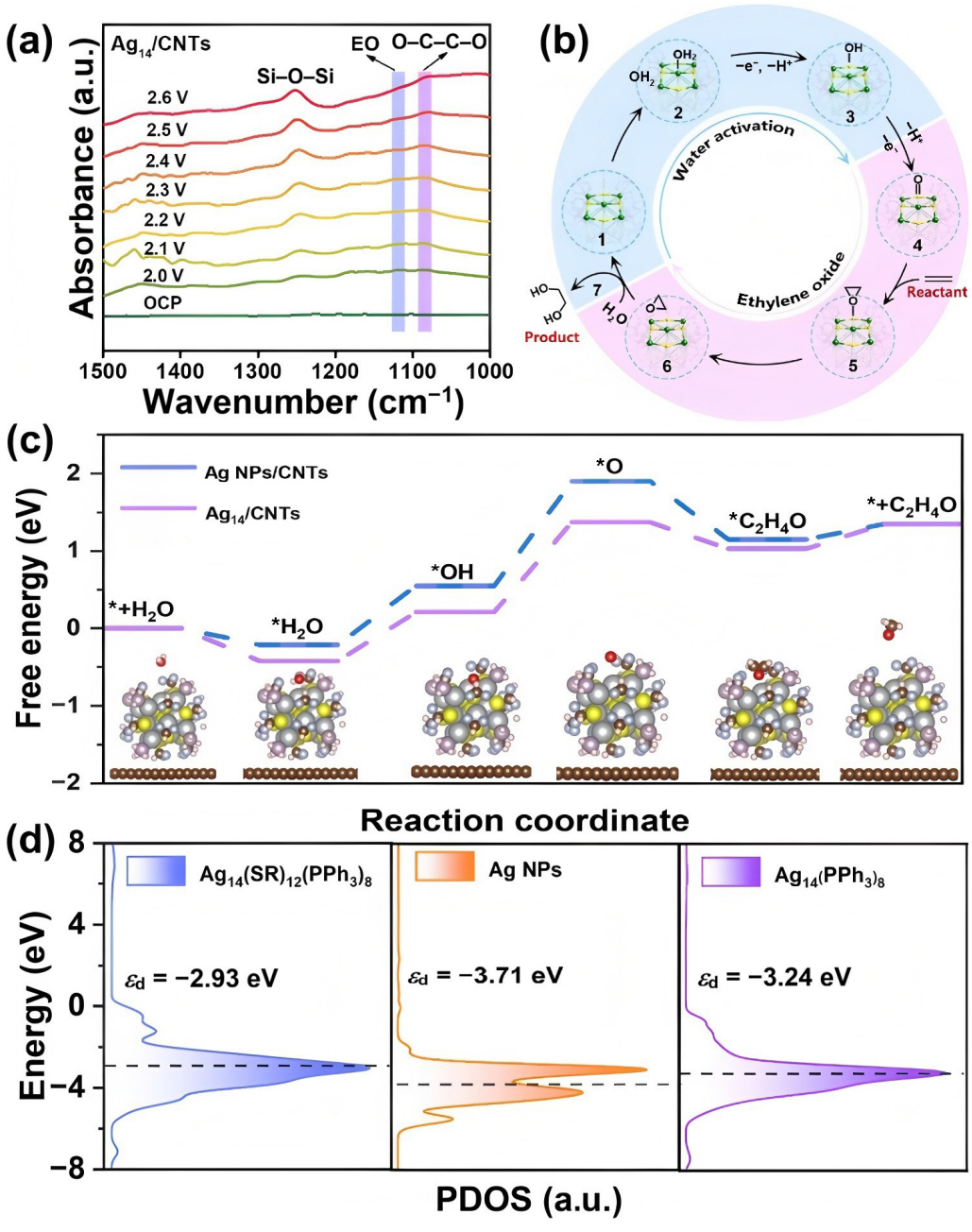

Figure 5 (a) *In situ* ATR-FTIR spectra of Ag_{14}/CNTs at different potential. (b) Reaction mechanism diagram of C_2H_4 to EG. (c) Free energy diagrams of C_2H_4 to EO on Ag NPs/CNTs and Ag_{14}/CNTs, and the adsorption configuration of the intermediate on Ag_{14}/CNTs. (d) The PDOS plots of $Ag_{14}(4\text{-}CF_3PhS)_{12}(PPh_3)_8$, Ag NPs, and $Ag_{14}(PPh_3)_8$.

attributable to the synergistic effect of the 4-CF_3PhS and PPh_3 ligands. Therefore, C_2H_4 and related intermediates exhibit lower adsorption free energy on Ag_{14}/CNTs, resulting in higher activity for the conversion of C_2H_4 to EG. Moreover, we calculated the charge distribution of Ag atoms in $Ag_{14}(4\text{-}CF_3PhS)_{12}(PPh_3)_8$ and $Ag_{14}(4\text{-}CF_3PhS)_{12}$. As shown in Fig. S34 and Table S4 in the ESM, the charge on Ag atoms in $Ag_{14}(4\text{-}CF_3PhS)_{12}(PPh_3)_8$ is higher than that in $Ag_{14}(4\text{-}CF_3PhS)_{12}$, indicating that the electron-donating effect of the mixed ligands is more effective in stabilizing the higher-valent silver. This facilitates the enhancement of the oxidative capacity of Ag-O species, thereby improving the catalytic activity for the conversion of C_2H_4 to EG [21, 22].

4 Conclusions

In summary, we synthesized an atomically precise $Ag_{14}S(4\text{-}CF_3PhS)_{12}(PPh_3)_8$ and loaded it onto CNTs for the conversion of C_2H_4 to EG. The Ag_{14}/CNTs achieved high EG productivity (73.43 μmol·h^{-1}), selectivity (> 96%) and turnover frequency (5.25 s^{-1}) at 2.4 V (vs. RHE). *In situ* characterization and theoretical calculations indicated that the catalytic process involves electrochemical activation of water to generate Ag-oxygen species, followed by the oxidation of C_2H_4 to form the intermediate EO, and eventually ring-opening of EO to EG. The enhanced catalytic performance of Ag_{14}/CNTs is primarily attributed to the electro-donating effect of mixed ligands effectively stabilize the high-valent silver species and shift the d-band center upward, thereby lowering

the RDS energy barrier and suppressing competitive OER. This work elucidates the structure-activity relationship of silver cluster catalysts in the electrocatalytic C_2H_4 to EG conversion, providing insights for the design of highly efficient cluster-based catalysts for organic transformations.

Electronic Supplementary Material: Supplementary material (crystal structure, TEM images, EDS mapping, partial catalytic performance, calculation model, and Tables S1–S4) is available in the online version of this article at a https://doi.org/10.26599/NR.2026.94908966.

Data availability

All data needed to support the conclusions in the paper are presented in the manuscript and the Electronic Supplementary Material.

Acknowledgements

This work was supported by the National Natural Science Foundation of China (No. 22471244), Key Basic Research of Henan (No. 252310420200), and the Zhongyuan Thousand Talents (Zhongyuan Scholars) Program of Henan Province (No. 234000510007). The Center of Advanced Analysis & GeneSequencing of Zhengzhou University was thanked for ICP-OES testing.

Declaration of competing interest

All the contributing authors report no conflict of interests in this work.

Author contribution statement

Y.-K. L.: Investigation, visualization, writing original draft, writing – review & editing. M.-Y. G.: Investigation. W.-T. L.: Investigation. Y.-R. G.: Investigation. M.-J. W.: Investigation. J. Z. D.: Supervision. R.-W. H.: Conceptualization, funding acquisition, supervision, resources, methodology, project administration. S.-Q. Z.: Funding acquisition, supervision, resources, project administration. All the authors have approved the final manuscript.

Use of AI statement

None.

References

[1] Xia, R.; Chen, Y. Q.; Chang, Y. X.; Shin, H.; Ze, H. J.; Liu, H. Z.; Ou, P. F.; Dorakhan, R.; Park, S.; Papangelakis, P. et al. Electrosynthesis of ethylene glycol from ethylene coupled with CO_2 capture. *Nat. Catal.* **2025**, *8*, 833–842.

[2] Pu, T. C.; Tian, H. J.; Ford, M. E.; Rangarajan, S.; Wachs, I. E. Overview of selective oxidation of ethylene to ethylene oxide by Ag catalysts. *ACS Catal.* **2019**, *9*, 10727–10750.

[3] Huang, L. S.; Bao, D. Y.; Zheng, Y.; Qiao, S. Z. Electrocatalytic production of ethylene glycol from ethylene on both electrodes. *ACS Energy Lett.* **2025**, *10*, 3907–3913.

[4] Yang, H. L.; Li, G. G.; Ma, W.; Hao, B. Y.; Zhang, Z. S.; Liu, Y. V.; Hao, Z. P. Recent developments in heterogeneous catalyzed epoxidation of ethylene to ethylene oxide. *Chem. —Eur. J.* **2025**, *31*, e202404773.

[5] Chung, M.; Jin, K.; Zeng, J. S.; Manthiram, K. Mechanism of chlorine-mediated electrochemical ethylene oxidation in saline water. *ACS Catal.* **2020**, *10*, 14015–14023.

[6] Yang, Y.; Wan, Y. Y.; Yan, N. Mediated electrosynthesis for greener ethylene glycol production. *Chem Catal.* **2025**, *5*, 101549.

[7] Li, X. W.; Yang, C. Y.; Tang, Z. Y. Electrifying oxidation of ethylene and propylene. *Chem. Commun.* **2024**, *60*, 6703–6716.

[8] Fan, L.; Zhao, Y. L.; Chen, L.; Chen, J. Y.; Chen, J. M.; Yang, H. Z.; Xiao, Y. K.; Zhang, T. Y.; Chen, J. Y.; Wang, L. Selective production of ethylene glycol at high rate via cascade catalysis. *Nat. Catal.* **2023**, *6*, 585–595.

[9] Huang, L. S.; Zheng, Y.; Qiao, S. Z. Challenges and opportunities in the electrochemical production of ethylene glycol. *Chem Catal.* **2026**, *6*, 101625.

[10] Liang, N. N.; Wang, H. B.; Wei, Y.; Wang, T.; Yu, W. H.; Yin, Z. H.; Zhao, Y.; Mao, T. T.; Han, J. R.; Zhao, Y. Y. et al. Arraying faceted manganese oxides for selective ethylene electro-oxidation to ethylene glycol in aqueous electrolytes. *Nat. Commun.* **2026**, *17*, 290.

[11] Asia to dominate Global Ethylene Glycol Capacity Additions by 2026. Offshore Technology. 2026.

[12] Yue, H. R.; Zhao, Y. J.; Ma, X. B.; Gong, J. L. Ethylene glycol: Properties, synthesis, and applications. *Chem. Soc. Rev.* **2012**, *41*, 4218–4244.

[13] Rebsdat, S.; Mayer, D. Ethylene glycol. In *Ullmann's Encyclopedia of Industrial Chemistry*; 7th ed. Wiley-VCH: Weinheim, 2000.

[14] Rebsdat, S.; Mayer, D. Ethylene oxide. In *Ullmann's Encyclopedia of Industrial Chemistry*. Wiley-VCH, 2001.

[15] Li, A. Z.; Yuan, B. J.; Xu, M.; Wang, Y.; Zhang, C. Y.; Wang, X. B.; Wang, X.; Li, J.; Zheng, L. R.; Li, B. J. et al. One-step electrochemical ethylene-to-ethylene glycol conversion over a multitasking molecular catalyst. *J. Am. Chem. Soc.* **2024**, *146*, 5622–5633.

[16] Chen, H. J.; Shin, H.; Huang, J. E.; Liu, H. Z.; Miao, R. K.; Xia, R.; Ni, W. Y.; Yu, J. Q.; Liang, Y. X.; Peng, B. S. et al. Electrolysis of ethylene to ethylene glycol paired with acidic CO_2-to-CO conversion. *Energy Environ. Sci.* **2025**, *18*, 8600–8607.

[17] Yu, J. Q.; Musgrave III, C. B.; Chen, Q. C.; Yang, Y.; Tian, C.; Hu, X. B.; Su, G. C.; Shin, H.; Ni, W. Y.; Chen, X. Q. et al. Ruthenium-substituted polyoxoanion serves as redox shuttle and intermediate stabilizer in selective electrooxidation of ethylene to ethylene glycol. *J. Am. Chem. Soc.* **2024**, *146*, 32660–32669.

[18] Wang, J.; Chen, Y. H.; Wang, Y. D.; Zhao, H.; Ye, J. Y.; Cheng, Q. Q.; Yang, H. Manipulating the electronic state of ruthenium to boost highly selective electrooxidation of ethylene to ethylene glycol in acid. *Chin. J. Catal.* **2024**, *60*, 376–385.

[19] Lum, Y.; Huang, J. E.; Wang, Z. Y.; Luo, M. C.; Nam, D. H.; Leow, W. R.; Chen, B.; Wicks, J.; Li, Y. C.; Wang, Y. H. et al. Tuning OH binding energy enables selective electrochemical oxidation of ethylene to ethylene glycol. *Nat. Catal.* **2020**, *3*, 14–22.

[20] Li, A. Z.; Wang, X. B.; Li, S. W.; Yuan, B. J.; Wang, X.; Li, R. P.; Zhang, L.; Li, B. J.; Duan, H. H. Direct electrooxidation of ethylene to ethylene glycol over 90% faradaic efficiency enabled by Cl^- modification of the Pd surface. *J. Am. Chem. Soc.* **2025**, *147*, 10493–10503.

[21] Yuan, B. J.; Xu, S. M.; Liu, X.; Li, A. Z.; Wang, X.; Shi, Q. J.; Li, R. P.; Zhang, C. Y.; Zhao, X. K.; Zheng, J. Y. et al. Homogeneous silver catalyst for propylene electrooxidation to propylene glycol. *Nat. Commun.* **2025**, *16*, 10319.

[22] Wang, X.; Xu, S. M.; Li, A. Z.; Yuan, B. J.; Shi, Q. J.; Liu, X.; Xu, M.; Liu, Y. H.; Kong, K. J.; Zhang, C. Y. et al. Ligand tuning of molecular ag catalysts enables efficient direct propylene electrooxidation to propylene glycol. *J. Am. Chem. Soc.* **2025**, *147*, 23090–23102.

[23] Holbrook, L. L.; Wise, H. Electrooxidation of olefins at a silver electrode. *J. Catal.* **1975**, *38*, 294–298.

[24] Li, X. W.; You, X. Y.; Yan, Z.; Yang, C. Y.; Zuo, L. L.; Huang, X.

W.; Chang, L.; Lu, S. Y.; Tang, Z. Y. Ag-doped Pd nano-dendritic for promoting the electrocatalytic oxidation of ethylene to ethylene glycol. *Mater. Chem. Front.* **2023**, *7*, 1437–1445.
[25] Du, Y. X.; Sheng, H. T.; Astruc, D.; Zhu, M. Z. Atomically precise noble metal nanoclusters as efficient catalysts: A bridge between structure and properties. *Chem. Rev.* **2020**, *120*, 526–622.
[26] Liu, X.; Cai, X.; Zhu, Y. Catalysis synergism by atomically precise bimetallic nanoclusters doped with heteroatoms. *Acc. Chem. Res.* **2023**, *56*, 1528–1538.
[27] Jing, W. T.; Shen, H.; Qin, R. X.; Wu, Q. Y.; Liu, K. L.; Zheng, N. F. Surface and interface coordination chemistry learned from model heterogeneous metal nanocatalysts: From atomically dispersed catalysts to atomically precise clusters. *Chem. Rev.* **2023**, *123*, 5948–6002.
[28] Pei, G. X.; Zhang, L. L.; Sun, X. Y. Recent advances of bimetallic nanoclusters with atomic precision for catalytic applications. *Coord. Chem. Rev.* **2024**, *506*, 215692.
[29] Liu, L. J.; He, J. Atomically precise coinage metal nanocluster photocatalysts: Recent advances in organic synthesis. *Aggregate* **2025**, *6*, e70226.
[30] Zhang, M.; Yang, F.; Zhu, M. S. Q.; Yao, Q. F. Electrocatalytic nitrate reduction promoted by atomically precise metal nanoclusters. *Chem. Res. Chin. Univ.* **2025**, *41*, 1485–1503.
[31] Song, T. X.; Shen, C. Y.; Tian, Y. Q.; Zhai, Q. X.; Tang, S. S.; Zhu, Y. A heterodimeric cluster-based pair catalyst for electrochemical synthesis of cyclohexanone oxime. *Angew. Chem., Int. Ed.* **2025**, *64*, e202507569.
[32] Zhang, B.; Long, Z. C.; Xu, J. R.; Xu, H. Y.; Wang, Q. M. Ultrastable copper superatom. *J. Am. Chem. Soc.* **2026**, *148*, 2519–2528.
[33] Lu, J. Z.; Shen, C. Y.; Tian, Y. Q.; Zhai, Q. X.; Han, M. C.; Liu, X.; Zhu, Y. An atomically precise $Ru_1Au_6(TBBT)_6(PPh_3)_6$ cluster catalyst for ammonia production. *Angew. Chem., Int. Ed.* **2025**, *64*, e202516398.
[34] Dong, J. P.; Li, J. K.; Zhang, H.; Xu, Y.; Zhao, S. N.; Li, G.; Wang, R.; Li, B.; Zang, S. Q. Accurate thermal resection of atomically precise copper clusters to achieve near-IR light-driven CO_2 reduction. *Adv. Mater.* **2025**, *37*, 2417747.
[35] Yan, X.; Xie, H. W.; Wu, G.; Xiao, F. X. Boosted solar water oxidation steered by atomically precise alloy nanocluster. *Chin. Chem. Lett.* **2025**, *36*, 110279.
[36] Pei, C.; Zhuang, S. L.; Wu, Z. K. Tailoring metal nanoclusters for enhanced electrocatalytic reduction of CO_2 to CO. *Aggregate* **2026**, *7*, e70272.
[37] Zhang, Z. P.; Yin, R. R.; Song, Z. Y.; Zhang, M. X.; Zhang, B. H.; Lu, S. S.; Yao, Q. F.; Jiang, D. E.; Xie, J. P.; Hu, W. P. Efficient electrocatalytic semi-hydrogenation of alkynes by interfacial engineering of atomically precise silver nanoclusters. *Angew. Chem., Int. Ed.* **2025**, *64*, e202500389.
[38] Liu, L. J.; Wang, Z. Y.; Wang, Z. Y.; Wang, R.; Zang, S. Q.; Mak, T. C. W. Mediating CO_2 electroreduction activity and selectivity over atomically precise copper clusters. *Angew. Chem., Int. Ed.* **2022**, *61*, e202205626.
[39] Chen, H.; Qi, K. S.; Dong, X. Y.; Pei, Y. N.; Jin, Y. J.; Zhang, H.; Li, S.; Wu, J.; Cai, J. M.; Zang, S. Q. Ligand-mediated activity of Cu_4 clusters boosts electrocatalytic nitrate reduction. *Angew. Chem., Int. Ed.* **2025**, *64*, e202510429.
[40] Zhu, X. J.; Si, W. D.; Qu, K. Y.; Song, L. Y.; Wang, J.; Gong, Y. S.; Sun, D.; Liu, X.; Wang, A. L. Nonmetallic modified atomically precise octagold nanoclusters for electrocatalytic nitrate reduction to ammonia. *J. Am. Chem. Soc.* **2025**, *147*, 44437–44446.
[41] Wang, P.; Xu, T. Y.; Xiong, S. L.; Wang, Y.; Sun, D.; Song, N.; Feng, J. K.; Xi, B. J. Ligand engineering‐enhanced catalytic activity of octanuclear Zn(II)-siloxane clusters for advanced lithium-sulfur batteries. *Angew. Chem., Int. Ed.* **2025**, *64*, e202516197.
[42] Nan, Z. A.; Wang, Y.; Chen, Z. X.; Yuan, S. F.; Tian, Z. Q.; Wang, Q. M. Catalyzed assembly of hollow silver-sulfide cluster through self-releasable anion template. *Commun. Chem.* **2018**, *1*, 99.
[43] Zhu, S.; Ding, L. T.; Zhang, X. H.; Wang, K.; Wang, X.; Yang, F.; Han, G. Y. Biaxially-strained phthalocyanine at polyoxometalate@carbon nanotube heterostructure boosts oxygen reduction catalysis. *Angew. Chem., Int. Ed.* **2023**, *62*, e202309545.
[44] Lv, Y. K.; Han, Y.; Wang, K.; Sun, W. Y.; Du, C. X.; Huang, R. W.; Peng, P.; Zang, S. Q. Satellite Pd single-atom embraced AuPd alloy nanoclusters for enhanced hydrogen evolution. *ACS Nano* **2024**, *18*, 32186–32195.
[45] Chen, Z. Y.; Walsh, A. G.; Wei, X.; Zhu, M. Z.; Zhang, P. Site‐specific electronic properties of $[Ag_{25}(SR)_{18}]^-$ nanoclusters by x‐ray spectroscopy. *Small* **2021**, *17*, 2005162.
[46] Lv, Y. K.; Wang, K.; Sun, W. Y.; Peng, P.; Zang, S. Q. A universal electrochemical synthetic strategy for the direct assembly of single‐atom catalysts. *Adv. Sci.* **2023**, *10*, 2304656.
[47] Lv, Y. K.; Wang, K.; Du, C. X.; Huang, R. W.; Zang, S. Q.; Peng, P. Sulfur-stabilized superfine Pt clusters synergized with single-atom Ni–N_4 sites for hydrazine oxidation-assisted hydrogen production. *Adv. Mater.* **2026**, *38*, e16082.
[48] Shen, S.; Wang, X. L.; Ding, Q.; Jin, S. Q.; Feng, Z. C.; Li, C. Effect of Pt cocatalyst in Pt/TiO_2 studied by *in situ* FTIR of CO adsorption. *Chin. J. Catal.* **2014**, *35*, 1900–1906.
[49] Ketchie, W. C.; Murayama, M.; Davis, R. J. Promotional effect of hydroxyl on the aqueous phase oxidation of carbon monoxide and glycerol over supported Au catalysts. *Top. Catal.* **2007**, *44*, 307–317.
[50] Mavrikakis, M.; Hammer, B.; Nørskov, J. K. Effect of strain on the reactivity of metal surfaces. *Phys. Rev. Lett.* **1998**, *81*, 2819–2822.